WILEY-VCH

Hybrid Hydrogel-Magnet Actuators with pH-responsive Hydrogels for Gastrointestinal Microrobots

*Yung Priscilla Lai, Zhaoxin Li, Hani Naguib, Eric Diller**

Y.P. Lai, Z. Li, H. Naguib, and E. Diller

Department of Mechanical and Industrial Engineering, University of Toronto, 170 College St., Toronto, M5S 3E3, Canada

E. Diller

Robotics Institute, University of Toronto, 55 St. George St. Toronto, M5S 0C9 Canada.

E. Diller

Institute of Biomedical Engineering, University of Toronto, 164 College St., Toronto, M5S 3E2, Canada

Email Address: eric.diller@utoronto.ca

E-mail: ediller@mail.utoronto.ca

Keywords: *hydrogel actuator, magnetic mechanism, pH-responsive hydrogel*

Limited space on millimeter-scale devices for biomedical applications makes it challenging to incorporate bulky actuators and power for onboard mechanical actuation. Stimuli-responsive hydrogels, such as pH-responsive hydrogels, provide a solution to automatically sense and actuate in the gastrointestinal tract. However, hydrogels are often non-load bearing and slow in actuation. To overcome these challenges, a new type of hybrid actuator is developed which utilizes a pH-responsive hydrogel with magnets to trigger magnetic springs (i.e., permanent magnets with repulsive, spring-like forces) to quickly initiate rotational and translational movements at pH > 6. The agar-poly(acrylic acid) hydrogel undergoes large volume transition at pH > 6 and exhibits large nominal blocking stress of 610 – 819 kPa for a 3 - 4 mm diameter cylinder hydrogel. Moreover, the scaling of hydrogel force and response times are experimentally confirmed. Based on the hydrogel properties, an analytical hydrogel model is developed to predict hydrogel force and displacement under varying magnetic loads and wall constraints in simulated gastric fluid (SGF, pH 1.2) and simulated intestinal fluid (SIF, pH 6.8), and the experimental data validates the model. Finally, an innovative hybrid hydrogel-magnet actuator that triggers rotational and translational motion without external activation is demonstrated.

1. Introduction

Stimuli-responsive hydrogels provide a promising approach to create miniaturized hydrogel actuators that can operate in remote locations without requiring any external control for activation. Moreover, they have been shown to exhibit responsiveness to stimuli such as temperature, [1-7] light, [4, 8, 9] humidity, [4, 10] solvent, [5, 11] and pH [2, 12] which lowers the complexity in the external control of these devices and provides opportunity to add more onboard capabilities in a compact space. Furthermore, their soft, gel-like property and great biocompatibility, have made them the primary choice to interface with biological environments such as in tissue engineering and drug delivery. [13, 14] In particular, the distinct pH regions in the gastrointestinal tract makes pH-responsive hydrogels a suitable candidate for actuation in gastrointestinal microrobots.

The pH-responsive hydrogel must possess robust mechanical properties for load bearing and displacement purposes for effective actuation via volumetric swelling. Hydrogel volumetric swelling is preferred because it can generate large displacement and blocking force compared to bimorph-like bending where there is a trade-off between blocking force and displacement via bending. [15] Regardless of actuation mode, the hydrogel's stiffness (Young's modulus) is typically low and measured in tens to hundreds of kilopascals. [14] Consequently, direct hydrogel actuation of a mechanism or spring will be limited by the hydrogel's stiffness and the mechanism speed will be highly dependent on the hydrogel swelling rate. Thus, a pH-responsive hydrogel with robust and load bearing properties that triggers a fast mechanism response is desired.

Pairing the hydrogels with magnets provides a solution to trigger fast, high energy density magnetic mechanisms via hydrogel swelling, similar to previous work using shape memory alloys and magnetic mechanisms but without the need of an onboard power source. [16] Magnetic modeling and magnetic mechanism design have been thoroughly studied. [16, 17] However, a method to design these magnetic mechanisms that can automatically trigger in the small intestines via hydrogel actuation is still required.

To design magnetic mechanisms that can automatically trigger in the small intestines via hydrogel swelling, the critical hydrogel height at triggering should be located between the maximum hydrogel height in the stomach and in the small intestines. These maximum hydrogel heights can be predicted by developing a hydrogel analytical model using parameters derived from measured mechanical properties such as hydrogel swelling ratio, blocking force and compressive stress-strain relation. These properties help determine the hydrogel height, the maximum loads, and the elastic stress of the hydrogel, respectively. The

predicted hydrogel heights are then experimentally validated. Hydrogel scaling laws are also experimentally confirmed to estimate the blocking force and the response times if smaller hydrogel sizes are used. In doing so, this work provides a solid theoretical foundation for the design of a millimeter-scale hybrid hydrogel-magnet actuator using a robust, load bearing pH-responsive hydrogel to drive rotational and translational motion without external activation for gastrointestinal applications.

2. Results

2.1. Hydrogel Swelling, Blocking Force, and Scaling Law

This section briefly discusses the hydrogel swelling, blocking force, and scaling properties that are required to model the hybrid hydrogel-magnet actuator in the subsequent sections. The pH-responsive hydrogel used in the actuator consists of an interpenetrating network of agar and poly(acrylic acid). The poly(acrylic acid) contributes to the pH-responsiveness whereas the agar network acts as additional structural support in the hydrogel.

The volumetric free swelling ratio of the pH-responsive hydrogel (J) at equilibrium is calculated from experimental data by Equation 1 using the average density of the dry hydrogel ($\rho_{dry\ hydrogel}$ = 1.5 ± 0.00003 g·mL^{-1}, n = 3), and the fluid density was approximated as water (ρ_{water} = 1 g·mL^{-1}).

$$\text{Swelling ratio } (J) = \frac{m_{swell} - m_{dry}}{m_{dry}} * \frac{\rho_{dry\ hydrogel}}{\rho_{water}} \quad (1)$$

As **Figure 1(a)** shows, the volumetric free swelling ratio of the hydrogel is small under low pH values in a 0.01 M phosphate buffer, whereas large volume transitions are observed when the pH value is greater than 6. In addition, the hydrogel blocking forces along the vertical direction for different pH values are measured by constraining the vertical stretch during hydrogel swelling and reporting the equilibrium force value. The nominal blocking stress is then computed by dividing the measured blocking force by the initial circular base area of the dry hydrogel. Figure 1(b) shows the nominal blocking stress of the hydrogel under different pH values in 0.01 M phosphate buffer. At pH > 6, there is large nominal blocking stress of 610 – 819 kPa. The hydrogel analytical model predicting the nominal blocking stress at various pH in a 0.01 M salt concentration is also plotted in Figure 1(b) and fits well with the experimental data. The hydrogel analytical model is described in the Supplementary Information and is based on a free energy balance of the hydrogel swelling at equilibrium in a solvent as seen in Illeperuma *et al.*[21] The total free energy of the swelled hydrogel at equilibrium is the summation of the free energy from polymer network stretching

counteracting the free energy contributions of solvent, ions, and electrostatic repulsion of the polymer chains in the hydrogel depending on the pH and salt concentration of the solvent. Next, the effect of the hydrogel's thicknesses and surface areas on blocking force and response times are investigated to confirm hydrogel scaling laws and plotted as scatter plots. Figure 1(c) and 1(d) show the measured blocking force of the cylinder shaped hydrogel in DI water with respect to the initial thickness and initial circular base area, respectively. It is observed that the blocking force is invariant to the initial thickness. The 95% confidence interval of the slope in Figure 1(c) (n = 9) is between -0.19 and 0.23, supporting that there is no correlation between hydrogel blocking force and its thickness as a slope of zero is possible. However, blocking force is proportional to the initial circular base area of the hydrogel. The 95% confidence interval of the slope in Figure 1(d) (n = 8) is between 0.068 and 0.11, supporting that there is a positive correlation between hydrogel blocking force and its circular base surface area. Meanwhile, the response time, which represents the time it takes for the hydrogel to reach a steady blocking force, is proportional to the initial curved surface area which is the contact surface area with the surrounding fluid (shown as Figure 2(e)). The 95% confidence interval of the slope in Figure 1(e) (n = 14) is between 0.25 and 0.96, supporting that there is a positive correlation between hydrogel response time and initial curved surface area. The hydrogel blocking force and response time scaling trends align with previously established hydrogel scaling laws as seen in Tanaka et *al*. [18] and Yuk et *al*.[19]

2.2. Magnetic Force Modeling vs. Experiment

A magnetic load will be applied on the hydrogels in the actuator. Thus, this section briefly shows the magnetic force between two permanent magnets modeled by a magnetic dipole model [20] and finite element analysis (FEA) as a function of the separation distance (Figure 1(f)). Experimental measurement is also provided to support the use of the magnetic models in Figure 1(f). The two magnets emulate the latch and actuating magnet in the hybrid actuator. In the magnetic dipole model, each cube magnet has a side length of 3 mm and is divided into 20 x 20 small components along its width and height. Each component can be approximated as a magnetic dipole and the overall magnetic force between two magnets is the sum of the interaction force between each pair of the dipoles. It is noted from the dipole model that the magnetic force is inversely proportional to r^4 and decays quickly as the separation distance increases. If the hydrogel and magnets are scaled down by 10x the characteristic length, the blocking force of the hydrogel and the magnetic force would decrease by 100x (Figure 1(d)) and 1000x (according to magnetic dipole model [20]), respectively. Meanwhile, the hydrogel

response time would decrease by 100x (Figure 1(e)). Therefore, the hydrogel blocking force can still overcome the magnetic force to ensure the actuator still functions at smaller scales.

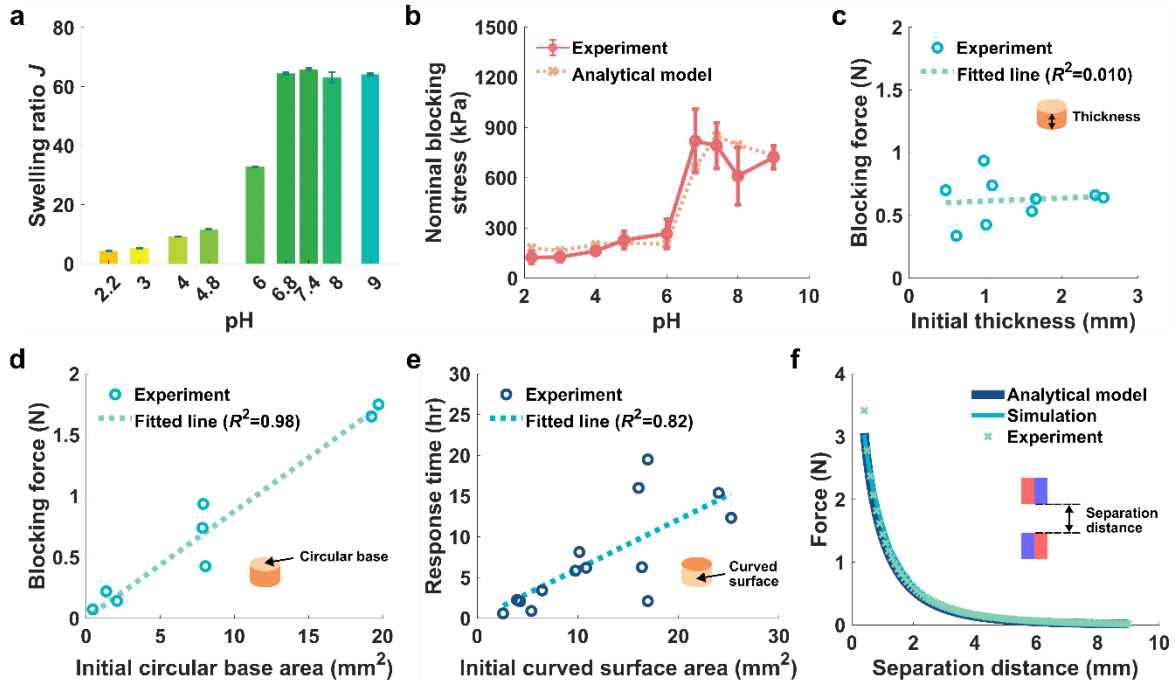

Figure 1. (a) Free swelling ratio of the hydrogel (J) under different pH values in 0.01 M phosphate buffer solution. (b) Nominal blocking stress measured from experiment and calculated from the hydrogel analytical model for different pH values in 0.01 M phosphate buffer solution. (c) Hydrogel blocking force as a function of the initial thickness in deionized water (DI water). (d) Hydrogel blocking force as a function of the initial circular base area in DI water. (e) Response time as a function of the initial curved surface area in DI water. (f) Magnetic force between two cube magnets calculated based on magnetic dipole model, simulation and measured from experiment. The side length of each cube magnet is 3 mm, and the separation distance is the distance between the closest faces of two magnets. Error bars are represented as standard error (n = 3).

2.3. Modeling the Stress and Stretch of a Constrained Hydrogel at Equilibrium

With key properties of the actuator including blocking force, free swelling ratio and compressive stress-strain relation known, an analytical hydrogel model can be derived as seen in the Supplementary Information. The constrained hydrogel force and stroke can then be determined and represented as the stress versus the vertical stretch ratio, as previously described in Illeperuma *et al.*[21] Only hydrogels with a cube geometry are used to limit the effect of deflection about the lateral axes when an anisotropic cross section is used (i.e.,

hydrogel bending). With isotropic dimension, the vertical displacement of the hydrogel is solely attributed to the hydrogel swelling and the stress of the cube in all principal directions can be easily determined using the hydrogel analytical model with homogeneous polymer networks.

In our model, the cube hydrogel is allowed to swell until the equilibrium is reached. The maximum stroke of the hydrogel can be achieved when the hydrogel swells freely without any load on it. Otherwise, if the hydrogel experiences constrained swelling, a blocking force that decreases with increasing stroke is generated along the constraint direction. Thus, the maximum blocking force is generated at zero stroke. The hydrogel stroke is described by its stretch ratio (λ_i) using the following equation,

$$\lambda_i = \frac{h_i}{h_0} \qquad (2)$$

where h_i is the swelled length of the hydrogel along direction *i* and h_0 is the initial dry length of the hydrogel along direction *i*. The direction *i* includes 1, 2 and 3, which represent *x*, *y* and *z* axes in a Cartesian coordinate system, respectively, as **Figure 2(a)** shows. Thus, the vertical stretch ratio, which represents the normalized hydrogel height over the initial dry hydrogel height along the principal direction *z*, is annotated as λ_3 and zero stroke is at $\lambda_3 = 1$. In addition, the wall constraint ratio (w_i) is expressed as,

$$w_i = \frac{d_i}{h_0} \qquad (3)$$

where d_i is the length of the wall constraint along direction *i*.

The blocking stress is plotted against λ_3 because the actuating magnet is pushed along axis 3. Three constraint cases on the hydrogel are studied. In the uniaxial constraint case, walls are constrained along axis 3 with varying d_3 and unconstrained along axis 1 and 2 (Figure 2(b)). When the fully swelled hydrogel contacts the top wall, $\lambda_3 = w_3$, the measured stress is the blocking stress. Otherwise, if the fully swelled hydrogel is less than the wall constraint, $\lambda_3 < w_3$, the blocking stress is zero. To calculate the stretches in the lateral direction when the hydrogel reaches the equilibrium with no lateral constraints, isotropic swelling is assumed ($\lambda_1 = \lambda_2$) and the true stress along lateral directions is zero ($\sigma_1 = \sigma_2 = 0$). Thus, one of the lateral stretch ratios λ_1 (or λ_2) can be expressed as a function of the vertical stretch ratio λ_3 by solving the following equation,

$$\sigma_1(\text{or } \sigma_2) = \sigma_{elastic} - \Pi_{ion} - \Pi_{mix+rep} = 0 \qquad (4)$$

where Π_{ion} is the osmotic pressure due to ions in the hydrogel, $\Pi_{mix+rep}$ is the osmotic pressure due to mixing of solvent and hydrogel and electrostatic repulsion. Subsequently, λ_1

(or λ_2) as a function of λ_3 is substituted into Equation 5 to solve the relation between the true stress in the vertical direction (σ_3) and the vertical stretch ratio (λ_3).

$$\sigma_3 = \sigma_{elastic} - \Pi_{ion} - \Pi_{mix+rep} \qquad (5)$$

Figure 2(c) shows the biaxial constraint case where walls are constrained along axis 1 with w_1 = 1 and along axis 3 with varying distances. The hydrogel is free to swell along axis 2, thus the true stress along d_2 is zero at equilibrium (σ_2 = 0). Meanwhile, the hydrogel will be fixed to the wall constraint along d_1 when the hydrogel swells, thus $\lambda_1 = w_1 = 1$. By substituting λ_1 and λ_2 into Equation 4 using the equation of σ_2 = 0, the lateral stretch ratio λ_2 can be expressed as a function of λ_3, which is then substituted into Equation 5 to derive the relation between the true stress σ_3 and the vertical stretch ratio λ_3.

Similarly, in the triaxial constraint scenario, the lateral constraints are fixed and the vertical constraint is changing with varying distances (Figure 2(d)). The vertical stretch ratio is computed the same way as the uniaxial constraint case if the fully swelled hydrogel does not contact the lateral wall constraints. Otherwise, the lateral stretch ratios will be fixed ($\lambda_1 = w_1$ = 2.79 and $\lambda_2 = w_2$ = 2.79) if the hydrogel at equilibrium reaches the wall constraints. With the lateral stretch ratios known, Equation 5 is used to calculate the true stress σ_3 at a specified λ_3.

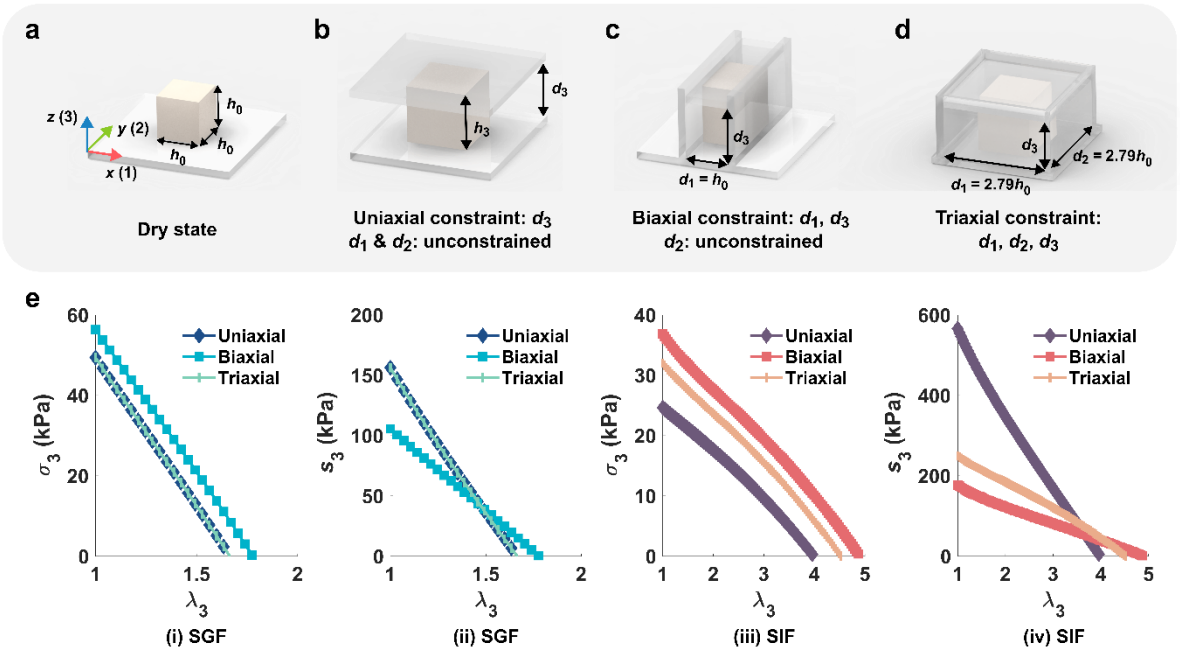

Figure 2. Illustration of the hydrogel in (a) dry state and under (b) uniaxial, (c) biaxial, and (d) triaxial wall constraints. (e) Predicted (i)(iii) true stress vs. vertical stretch ratio and (ii)(iv) nominal stress vs. vertical stretch ratio of a hydrogel with uniaxial, biaxial, and triaxial wall constraints in (i)(ii) simulated gastric fluid (SGF) and (iii)(iv) simulated intestinal fluid (SIF).

The actuator embedded with such pH-responsive hydrogel can prospectively operate in the gastrointestinal tract due to distinct pH values in the stomach and the intestine. Therefore, the swelling of the hydrogel is evaluated in both simulated gastric fluid (SGF, pH 1.2 & ~0.05 M salt) and simulated intestinal fluid (SIF, pH 6.8 & ~0.1 M salt) environments using the hydrogel model. The relation between the true stress σ_3 and the vertical stretch ratio λ_3 is computed for different constraint cases using the hydrogel analytical model discussed above. Meanwhile, the nominal stress in the vertical direction s_3, which is the first Piola-Kirchhoff stress, is computed using the following equation,

$$s_3 = \lambda_1 \lambda_2 \sigma_3 \quad (6)$$

Figure 2(e) shows the predicted true stress-stretch and nominal stress-stretch plots of the hydrogel under different constraint and fluid conditions. For all plots in Figure 2(e), the stress at $\lambda_3 = 1$ represents the maximum blocking stress of the hydrogel at zero stroke (y-intercept), while the vertical stretch ratio at $\sigma_3 = 0$ (or $s_3 = 0$) represents the free stretch ratio along axis 3 (x-intercept). In SGF where the pH value is small, the free swelling ratio of the hydrogel is small, thus the hydrogel at equilibrium under triaxial constraint does not reach the lateral constraints. Therefore, the vertical stress is the same as the uniaxial constraint condition and the stress curves of these two cases overlap each other, which is shown as Figure 2(e)(i) and 2(e)(ii).

In comparison, larger true stress can be observed for the biaxial constraint case in SGF due to tight wall constraint of $w_1 = 1$ along axis 1 similar to what was discussed in Na *et al.* [22] The wall constraint lowers the elastic polymer network stretching stress in the hydrogel that opposes the osmotic pressure from the ions, solvent, and any electrostatic repulsion in the polymer network, leading to net increases in hydrogel blocking stress. Therefore, larger true stress can be obtained by applying constraints to the hydrogel without implementing chemical modifications.

In SIF where the pH value is large, the dimension of the hydrogel at equilibrium is larger than that in SGF. Again, by applying constraints on the hydrogel, larger true stress can be achieved as observed with the biaxial and triaxial constraints versus the uniaxial constraints in SIF. Meanwhile, the biaxial constraint has slightly larger true stress than the triaxial constraint because of the tighter wall constraint of $w_1 = 1$ than the wall constraint of $w_1 = w_2 = 2.79$ which is approaching the free swelling stretch of the hydrogel of 3.43 ± 0.05 (based on the experimentally measured free swelling ratio in SIF, mean ± standard deviation, n = 3). Furthermore, the true stress of the hydrogel in SIF is smaller than that in SGF due to decreasing modulus of the hydrogel at high pH (Figure 2(e)(i) vs. 2(e)(iii), Figure S1 and S3).

The true stress is then converted to the nominal stress to evaluate whether the hydrogel force can overcome magnetic load in the next section. It can be seen from Figure 2(e)(ii) and 2(e)(iv) that for both SGF and SIF, less constrained hydrogel tends to have larger nominal stress due to larger lateral stretch ratios in Equation 6. For instance, the hydrogel in the uniaxial constraint can achieve free swelling along lateral directions in SIF and can achieve higher λ_1 and λ_2 values than the other two cases with lateral constraints. By understanding the hydrogel stress and swelling under different constraints and pH environments, the hydrogel force and displacement in the hybrid hydrogel-magnet actuator can be predicted in the next section.

It is noted that the viscoelastic behaviors of the hydrogel can be neglected in the hydrogel analytical model discussed above because the stress-stretch curve of the hydrogel (Figure 2(e)) is when the hydrogel is at equilibrium. Therefore, the hydrogel stress-strain behavior will no longer be time-dependent. Furthermore, the storage modulus (G') and the loss modulus (G'') of the hydrogel remains relatively constant under low strain as observed from the amplitude sweep of the hydrogel in Figure S3, which demonstrates the overall elastic, solid-like property of the hydrogel at low strains over the pH range from 2.2 to 7.4.

2.4. Constrained Hydrogel Swelling with and without Magnetic Load

Based on the stress-stretch curves in the previous section, the vertical stretch ratios of the hydrogel with and without magnetic load can be predicted and can be experimentally confirmed by placing the hydrogel in a 3D printed square tube with lateral constraints of $w_1 = w_2 = 2.79$ in both SGF and SIF environments, which is shown as **Figure 3(a)**. The initial side length of the dry hydrogel is 1.42 mm, and the hydrogel is not bound to the surrounding rigid surfaces.

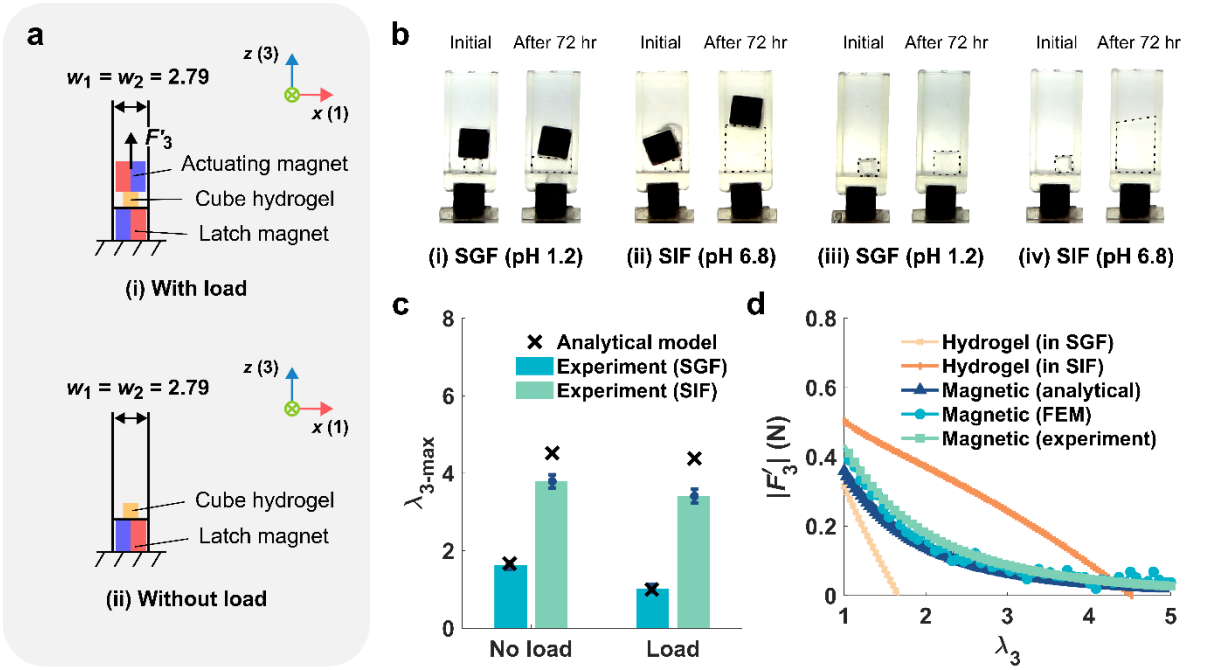

Figure 3. (a) Illustration of the cube hydrogel in the square tube (i) with and (ii) without magnetic load. The lateral constraints for the hydrogel are $w_1 = w_2 = 2.79$. (b) Cube hydrogel swelling in simulated gastric fluid (SGF) or simulated intestinal fluid (SIF) for 72 hours (i)(ii) with and (iii)(iv) without magnetic load. All magnets are 3 mm cube magnets. Material edges are outlined by dotted lines. Slanted material edges are due to imperfections when fabricating the hydrogel. (c) Maximum vertical stretch ratios λ_{3-max} of the hydrogel predicted by the hydrogel analytical model and computed from experiments with and without magnetic load in SGF and SIF. Error bars are standard deviation. (d) Predicted hydrogel and magnetic force magnitude of two 3 mm cube magnets on the actuating magnet $|F'_3|$ vs. vertical stretch ratio of the hydrogel in SGF and SIF. Hydrogels are subject to wall constraints of $w_1 = w_2 = 2.79$ in the lateral directions.

For the case with magnetic load, the hydrogel is sandwiched by two 3 mm cube magnets. However, it is difficult to balance the 3 mm cube magnet on top of the 1.42 mm hydrogel cube in the experiment. Thus, as Figure 3(b) shows, the actuating magnet is slightly slanted in the tube at the initial state. The hydrogel initial height and the heights after 72 hours in both SGF and SIF were measured using imaging software to calculate the maximum vertical stretch ratio. For the case without magnetic load, the hydrogel was allowed to swell without the actuating magnet. It can be seen from Figure 3(b) that the hydrogel swelling in SIF is larger than that in SGF for both cases with and without magnetic load, which again demonstrates the larger swelling ratio at higher pH values.

2.4.1 Constrained Hydrogel Model vs. Experiment

The maximum vertical stretch ratios of the constrained hydrogel with and without magnetic load in both SGF and SIF are plotted as Figure 3(c) analytically and experimentally. For the case without magnetic load in SGF, the predicted λ_{3-max} based on the hydrogel analytical model is 1.67 (x-intercept of the triaxial constraint in Figure 2(e)(i) and 2(e)(ii)) while the experimental λ_{3-max} is 1.62 ± 0.10 (mean ± standard deviation). For SIF, the predicted λ_{3-max} is 4.49 (x-intercept of the triaxial constraint in Figure 2(e)(iii) and 2(e)(iv)) while the experimental λ_{3-max} is 3.79 ± 0.17 (mean ± standard deviation).

For the case with magnetic load, the maximum stretch ratios λ_{3-max} with magnetic load are smaller than those without magnetic load since the magnetic force opposes the hydrogel force along the vertical direction. Figure 3(d) compares the magnetic force and predicted hydrogel force magnitudes on the actuating magnet as the vertical stretch changes. The magnetic forces between two 3 mm cube magnets are plotted based on the magnetic dipole model, finite element analysis and experimental measurement, while the hydrogel force is the predicted force using the hydrogel analytical model. In SGF with magnetic load, the hydrogel force magnitude is consistently smaller than the magnetic force magnitude on the hydrogel. Therefore, no swelling occurs, and the predicted λ_{3-max} is 1, which is close to the experimental λ_{3-max} of 1.03 ± 0.09 in SGF as Figure 3(c) shows (mean ± standard deviation). In SIF with magnetic load, the hydrogel force is large enough to push the magnets apart and it decreases as the hydrogel stretches (Figure 3(d)). The hydrogel stops stretching when the magnetic and hydrogel forces intersect. The λ_3 in SIF at this intersection is the predicted λ_{3-max} under magnetic load and determined to be 4.33, which is slightly larger than the experimental value of 3.41 ± 0.18 (mean ± standard deviation).

The differences between the predicted and experimental λ_{3-max} may come from experimental errors such as batch-to-batch variation, parallax errors when measuring hydrogel height in the images, and wall frictions on the hydrogel at large swelling in SIF. In addition, the hydrogel analytical model was conventionally applied to a hydrogel bonded to the rigid surface and was relatively thin to ensure homogeneous swelling. [23] Moreover, SIF has a slightly higher salt concentration of 0.10 M compared to 0.05 M of SGF. The activities of the ions may need to be considered if higher salt concentrations are used to model the non-ideal solution as discussed in Hong *et al*. [24] Thus, less accurate predictions were observed in SIF compared to SGF (Figure 3(c)).

2.4.2 Unconstrained Hydrogel Model vs. Experiment in SGF and SIF

Other than the constrained swelling investigated above, free swelling tests were implemented in SGF and SIF to further observe the swelling of the hydrogel analytically and experimentally. The analytical free stretch ratios (i.e. stretching of the hydrogel under free swelling) are determined from the x-intercepts of the uniaxial constraint curve in Figure 2(e)(i) and 2(e)(iii), which are 1.67 and 4 for SGF and SIF. To determine the experimental free stretch ratios, volumetric swelling ratios are first computed as 4.72 ± 0.16 and 40.52 ± 1.64 (mean ± standard deviation, n = 3) in SGF and SIF, respectively using Equation 1. Based on the assumption of isotropic free swelling, the stretch ratios in all three directions would be the same and equal to,

$$\lambda_i = J^{1/3} \qquad (7)$$

where λ_i is the free stretch ratio. Using equation 7, the experimental free stretch ratios are computed as 1.68 ± 0.02 and 3.43 ± 0.05 (mean ± standard deviation, n = 3) for SGF and SIF, respectively, which showed relatively good model prediction.

2.4.3 Sizing the Initial Hydrogel Dimensions

The side length of the fabricated cube hydrogel is on average 1.42 mm. The magnetic force on the hydrogel may differ when the size and the magnetization of the magnets change. To ensure the hydrogel can initially displace the actuating magnet, the minimum initial side length of the cube hydrogel can be determined by,

$$h_{min} = \sqrt{\frac{F_m}{s}} \qquad (8)$$

where h_{min} is the minimum side length of the hydrogel in meters, F_m is the magnetic force on the hydrogel in Newtons, and s is the nominal blocking stress of the hydrogel in a known pH solution in Pascals. Equation 8 is based on stress equal to force over surface area where the surface area is of a cube hydrogel is a square. Since the nominal blocking stress is known given the pH value, the initial hydrogel size in the actuator is dependent on the magnetic force on the hydrogel F_m. The magnetic force can be calculated by the magnetic dipole model. Therefore, the initial length of the cube hydrogel h_0 should be greater than h_{min} to ensure the displacement of the actuating magnet. The use of the equation will be demonstrated in the following section.

2.5. Hybrid Hydrogel-magnet Actuator Design

The hybrid hydrogel-magnet actuator design coupled with simple mechanisms for rotational and translational motion is discussed in this section. **Figure 4(a)** shows the hybrid hydrogel-magnet actuator which comprises two magnets that sandwich an initially dry hydrogel. The two magnets are placed with magnetic moments parallel and opposite to each other, thus an attractive magnetic force is generated. The magnets are constrained in a square tube where the latch magnet is fixed at the bottom. The actuating magnet can be vertically displaced inside the tube to different heights via hydrogel swelling in varying pH solutions. A pH-activated, small-scale device is created by pairing the hybrid actuator with magnetic springs (referred to as spring magnets going forward). At pH > 6, the magnetic mechanism is triggered when the hydrogel swells to the critical hydrogel height.

The direction of motion of the spring magnet differs depending on how it is constrained. Figure 4(b) shows different motion scenarios of the spring magnet. In the rotational motion scenario, the spring magnet is fixed onto the end of a link that is connected to the hybrid actuator by a pin joint on the other end. As the hydrogel swells, the actuating magnet moves upwards and generates an increasing repulsive magnetic force on the spring magnet, which triggers the link to rotate about the pin joint. In the translational motion scenarios, the spring magnet is restricted to moving either horizontally or vertically. The increasing repulsive magnetic force between the actuating magnet and the spring magnet triggers the translational motion of the spring magnet as the hydrogel swells.

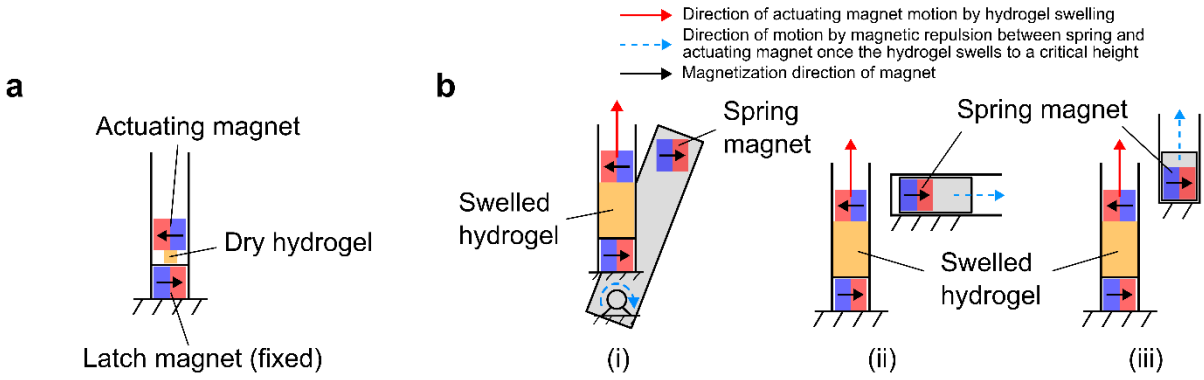

Figure 4. Hybrid hydrogel-magnet actuator and actuator coupled with spring magnets. (a) Schematic illustration of hybrid hydrogel-magnet actuator with an initially dry hydrogel. Black arrows represent the magnetic moment directions of the magnets. (b) Hybrid actuator coupled with spring magnets to generate (i) rotational motion, (ii) horizontal translational motion, and (iii) vertical translational motion. Red arrows represent the direction of motion of the actuating magnet as the hydrogel swells. The hydrogel swells and slides the actuating

magnet closer to the spring magnets. Blue dashed arrows represent the direction of rotation or motion of the link with spring magnet due to magnetic force repulsion between the spring and actuating magnet.

2.5 Demonstration of Rotational and Translational Motion with the Actuator

The known hydrogel properties and constrained hydrogel behaviors studied in the previous sections will now be used to design mechanisms of rotational and translational motion that are triggered via hydrogel swelling by coupling the hydrogel with spring magnets in a hybrid actuator. Since it is difficult to balance the large magnet on a small hydrogel as previously seen in Figure 3(b), the initial hydrogel wall constraints were set to $w_1 = 1$ and $w_2 = 2.79$ to ensure the actuating magnet can lie flat on top of the hydrogel (i.e., a trench houses the hydrogel as seen in **Figure 5(a)** and 5(d)). The device will be in SGF first to simulate the actuator going into the stomach, where the hydrogel swelling is small. Since the lateral stretch ratio λ_2 is less than the lateral constraint w_2 at equilibrium in SGF, the hydrogel swelling in SGF can be regarded as the biaxial constraint case as the hydrogel will still be constrained along axis 1 and 3. In SIF where the hydrogel swelling is large, the swelled hydrogel will be squeezed out of the initial tight constraints of the trench and will eventually be subjected to triaxial constraints. In SIF, the subsequent wall constraints are set to $w_1 = w_2 = 2.79$, which is the triaxial constraint case.

The mechanisms of the hybrid hydrogel-magnet actuators that drive rotational and translational motion are shown as Figure 5(a) and 5(d), respectively. The latch and actuating magnets are in the main column of the square tube separated by the hydrogel and two 0.5 mm spacers. In the rotational actuator, the initial position of the spring magnet's center of mass (COM) is 3.75 mm and 10 mm from the latch magnet's COM along axis 1 and 3, respectively. The magnet in the far bottom right does not interact with the spring magnet until it is triggered. For the translational actuator, the distances from the left and right spring magnets' COM to the latch magnet's COM are respectively -4.55 mm and 5 mm along axis 1 and both 9.75 mm along axis 3. The spring magnets in these actuators are all fixed for the force evaluation during hydrogel swelling.

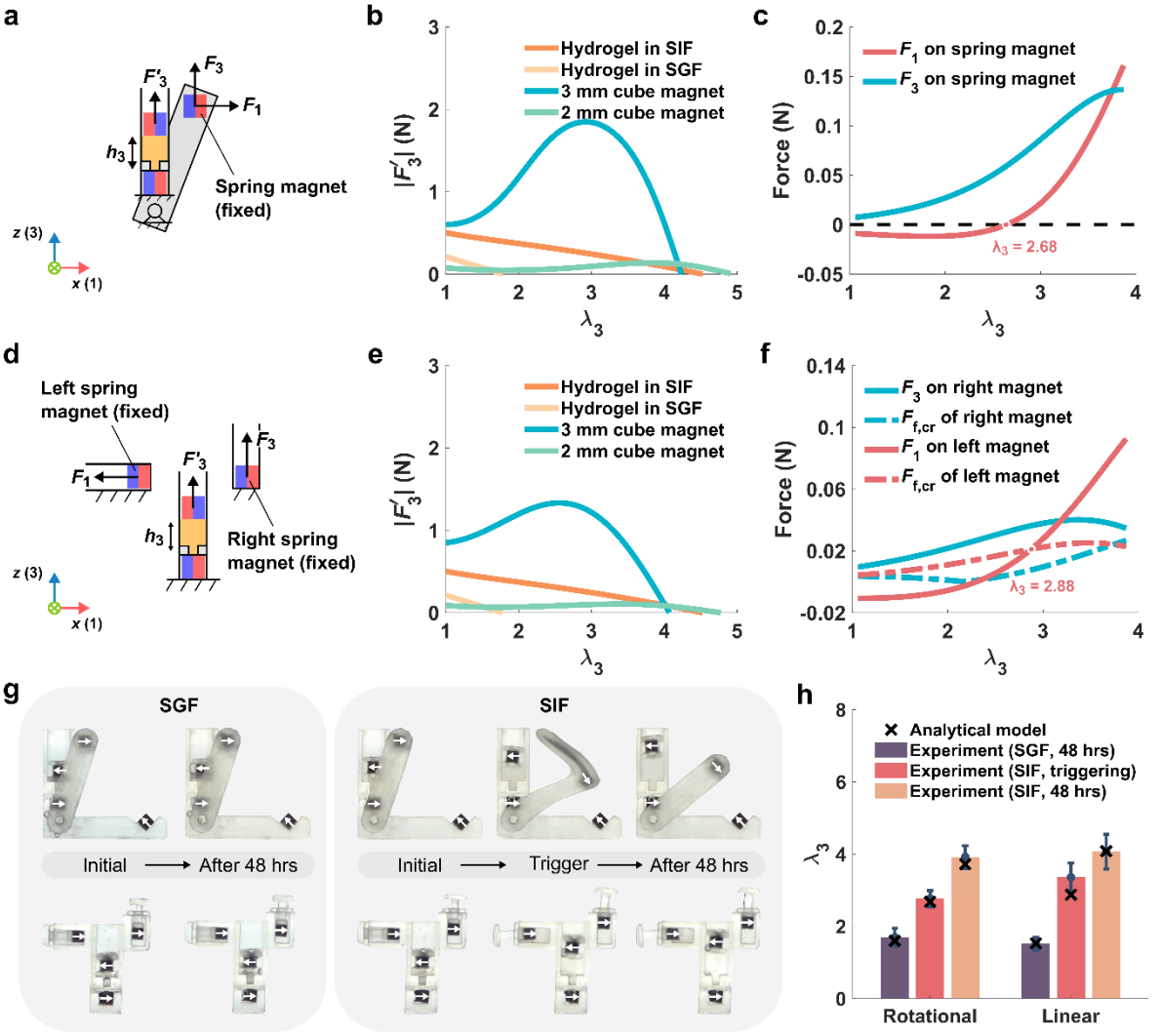

Figure 5. (a) Schematic illustration of the hybrid hydrogel-magnet actuator with rotational motion. The two small gray squares in the actuator tube makes the trench to initially place the hydrogel into and allow the actuating magnet to lay flat on top of the hydrogel. The trench has a height along axis 3 of 1.42 mm. (b) Magnitude of predicted magnetic and hydrogel blocking force on the actuating magnet $|F'_3|$ versus the vertical stretch ratio of the hydrogel λ_3 based on the magnetic dipole and hydrogel analytical model for the rotational mechanism. The magnetic forces are computed for both 2 mm and 3 mm cube magnets with fixed spring magnet. (c) Predicted vertical net magnetic force F_3 and horizontal net magnetic force F_1 on the spring magnet versus vertical stretch ratios λ_3 based on the magnetic dipole model for the rotational mechanism. All magnets are 2 mm cube magnets. (d) Schematic illustration of the hybrid hydrogel-magnet actuator that can generate translational motions horizontally and vertically. The two small gray squares in the actuator tube makes the trench to initially place the hydrogel into and allow the actuating magnet to lay flat on top of the hydrogel. The trench has a height along axis 3 of 1.42 mm. (e) Magnitude of predicted magnetic and hydrogel

blocking force on the actuating magnet $|F'_3|$ versus the vertical stretch ratio of the hydrogel λ_3 based on the magnetic dipole and hydrogel analytical model for the translational mechanism. The magnetic forces are computed for both 2 mm and 3 mm cube magnets with fixed spring magnets. (f) Predicted vertical net magnetic force F_3 on the right spring magnet and horizontal net magnetic force F_1 on the left spring magnet as well as critical friction forces on both spring magnets at varying vertical stretch ratios λ_3 based on the magnetic dipole model for the translational mechanism. All magnets are 2 mm cube magnets. (g) Response of hybrid hydrogel-magnet actuators in SGF and SIF at different moments in time. All magnets are 2 mm cube magnets. (h) Comparison of analytical and experimental vertical stretch ratios λ_3 of the hydrogel in SGF at 48 hours as well as in SIF at the triggering moment and 48 hours for rotational and translational mechanisms. Error bars are standard deviation.

2.5.1 Choosing the Magnet Size and Initial Hydrogel Size: Comparison of Magnetic and Hydrogel Blocking Force on the Actuating Magnet

The magnetic force and the hydrogel blocking force on the actuating magnet for both rotational and translational mechanisms are calculated to evaluate whether the swelled hydrogel can displace the actuating magnet. The hydrogel forces under the biaxial constraint in SGF (w_1 = 1, unconstrained along axis 2) as well as under the triaxial constraint in SIF are predicted ($w_1 = w_2 = 2.79$). The net magnetic forces on the actuating magnet are not only from the latch magnet as seen in Figure 3(d) but also from the spring magnets in the mechanism. Magnetic forces are computed using the magnetic dipole equation.[20] Cube magnets with 3 mm side length are first selected as the dimension for all magnets in the actuators. However, it is observed from Figure 5(b) and 5(e) that all hydrogel forces are smaller than the magnetic force and will not be able to displace the actuating magnet. Therefore, the dimensions of the cube magnets are changed to 2 mm since the 1.42 mm cube hydrogel can generate maximum blocking forces of 0.21 N and 0.50 N in SGF and SIF, respectively, which are greater than the initial magnetic forces on the 2 mm actuating cube magnet. Thus, the hydrogel will be able to displace the 2 mm actuating magnet slightly in SGF and displace it a lot more in SIF during hydrogel swelling for both rotational and translational mechanisms. Based on the force analysis, the dimension of all magnets in both rotational and translational mechanisms is set to 2 mm for the subsequent evaluations and experiments.

Another approach to displace the actuating magnet but not modify the dimensions of the magnets is to increase the initial side length of the cube hydrogel. Since the vertical stretch ratio under free swelling (λ_3 at $F_3 = 0$) is constant, assuming a linear F_3-λ_3 curve for the

hydrogel blocking force in SIF, a line can be drawn from the hydrogel vertical stretch ratio at F_3 = 0 (x-intercept of the hydrogel force in SIF in Figure 5(b) and 5(e)) to the tangent of the magnetic force curve for the 3 mm cube magnets. The drawn line should always be greater than the magnetic force to ensure the displacement of the actuating magnet by the hydrogel. By extending the line, the maximum blocking force of the hydrogel at λ_3 = 1 (zero stroke) can be estimated. The required hydrogel blocking forces in SIF are approximately 5.23 N and 2.83 N for the rotational and translational mechanisms, respectively. With the nominal blocking stress of the hydrogel at λ_3 = 1 in SIF known as 201.4 kPa (derived from the y-intercept of the triaxial constraint curve in Figure 2(e)(iv)), the minimum initial side length of the hydrogel can then be estimated as 5.1 mm and 3.75 mm for rotational and translational actuators, respectively, using Equation 8.

2.5.2 Ensuring the Mechanism Triggers in SIF: Analysis of Magnetic Force on the Spring Magnets

The critical hydrogel height at which the mechanism triggers is calculated and represented as λ_{3-crit}. In the rotational mechanism, the net magnetic forces on the spring magnet along horizontal and vertical directions are determined by analytically computing the magnetic force from the latch magnet and the actuating magnet during hydrogel swelling using the magnetic dipole model, which are shown in Figure 5(c). The rotational motion of the arm can be triggered when the horizontal net magnetic force on the spring magnet F_1 becomes positive as the hydrogel swells, thus generating a torque on the arm. The λ_{3-crit} for the rotational mechanism is 2.68 when F_1 crosses zero from the negative plane to the positive plane.

In the translational mechanism, there are two spring magnets which include the left spring magnet that moves horizontally (along axis 1) and the right spring magnet that moves vertically (along axis 3). The spring magnet can be triggered to move when the net magnetic force on the magnet exceeds the critical static friction force. The static coefficient of friction of the magnet against the actuator wall (c_f) is computed as 0.42 using the following equation based on an incline test,

$$c_f = \tan(\alpha). \qquad (9)$$

where α is the angle of incline.

The critical friction force of the magnet $F_{f,cr}$ is then determined by multiplying the coefficient with the normal force to the wall. It is observed from Figure 5(f) that the vertical net magnetic force on the right spring magnet F_3 is always greater than $F_{f,cr}$ as the hydrogel swells. Meanwhile, the gravity of the right magnet is negligible compared with the magnetic

repulsion along the vertical axis. Thus, the net force on the right magnet is always pointing upwards during hydrogel swelling, which contributes to the displacement of the magnet at the initial state. For the left spring magnet, the horizontal net magnetic force F_1 is smaller than $F_{f,cr}$ initially, thus the magnet is impeded from moving (Figure 5(f)). As the hydrogel swells, F_1 becomes greater and exceeds $F_{f,cr}$ at the critical vertical stretch ratio λ_{3-crit} = 2.88, the net force on the left magnet points leftwards and the translational motion is triggered.

Figure 5(g) shows the response of the rotational and translational mechanisms in SGF and SIF. In SGF, the rotational and translational mechanisms remain untriggered after 48 hours. In SIF, the rotational and translational motions are triggered as the hydrogel swells and displaces the actuating magnet upwards in the main column of the square tube. The time from the initial state to the moment of triggering is ~11 hours for the rotational mechanism and ~21 hours for the translational mechanism. After the triggering occurs, the hydrogel keeps swelling and pushes the right spring magnet to its fullest extent. The final hydrogel height at 48 hours is slightly larger than the critical hydrogel height.

2.5.3 Predicted vs. Experimental Vertical Stretch Ratio in SGF and SIF

Figure 5(h) compares the predicted and experimental vertical stretch ratios in SGF and SIF at equilibrium and in SIF at the triggering moment for the rotational and translational mechanisms. The predicted vertical stretch ratios at equilibrium are derived from the intersection of the hydrogel blocking force and the magnetic force of 2 mm magnets on the actuating magnet in Figure 5(b) and 5(e). In SGF, the predicted vertical stretch ratios λ_{3-max} are 1.6 and 1.53 for rotational and translational mechanisms respectively, which are similar to the experimental λ_{3-max} of 1.7 ± 0.24 and 1.52 ± 0.18 for rotational and translational mechanisms, respectively (mean ± standard deviation). In SIF, the predicted λ_{3-max} are 3.66 and 3.99 for the rotational and translational mechanisms respectively, which are similar to the experimental λ_{3-max} in SIF of 3.92 ± 0.31 and 4.07 ± 0.48 for the rotational and translational mechanisms, respectively (mean ± standard deviation).

In addition, the λ_{3-crit} are analytically predicted from Figure 5(c) and 5(f) as 2.68 and 2.88 for rotational and translational mechanisms, respectively, in SIF. The experimental λ_{3-crit} are 2.77 ± 0.22 and 3.36 ± 0.40 for rotational and translational mechanisms, respectively (mean ± standard deviation). It can be observed that all the predicted λ_3 values are close to or within the error bar of the λ_3 computed from experiments, which demonstrates the accuracy of our prediction model for the hydrogel swelling. Moreover, the λ_{3-crit} falls within the λ_{3-max} in SGF and λ_{3-max} in SIF and therefore, the mechanism is guaranteed to trigger in SIF. The video

demonstrating the triggering of the rotational and translational mechanisms in SIF is shown in the Supplementary Information.

2.5.4 Mechanism Output Force

While not in the scope of this paper, another property that will be of interest for these actuators and mechanisms is the mechanism output force. The output forces of the rotational and translational motion mechanisms solely depend on the net force of the spring magnet and is an area of further exploration. Some preliminary information on the theoretical actuator output force can be found in the Supplementary Information.

3. Conclusion

Using a combination of hydrogel and magnetic modeling, we were able to predict the critical hydrogel height to trigger the mechanism in SIF. The predicted hydrogel heights at equilibrium and at the triggering moment coincided well with the experimentally measured data. However, the applicability of the model was found to be limited to cube shaped hydrogels and at relatively low salt concentrations (0.01 – 0.1 M). Errors such as frictions and capillary forces on the spring magnet can cause slight deviation between the predicted and experimental values. Meanwhile, wall friction and contact mechanics between the wall and the hydrogel were not investigated in this work, which may also contribute to some differences between the experiment and the hydrogel analytical model. If hydrogel wall friction and contact mechanics can be accurately predicted, predicted hydrogel heights would lower in value for improved hydrogel height estimation. Furthermore, the time to reach the critical hydrogel height was 11 and 21 hours for the rotational and translational motion mechanism respectively. This time-to-trigger will need to be tuned if lower trigger times are desired by modifying the hydrogel chemical composition, synthesis procedures, or lowering the critical hydrogel height.

The hydrogel response time may be slow, but devices passively transiting through the body by the natural contractions of the gastrointestinal tract can take several hours which allows the hydrogel to swell to the critical height. The critical hydrogel height will be between the maximum swelling in the stomach and in the small intestines. For example, if the critical hydrogel height is smaller, the hydrogel swelling time can be lowered. Once the critical height is reached, the sliding joint or linkage mechanisms are triggered quickly and automatically for drug delivery and sampling applications in the small intestines.

In conclusion, it was observed that: i) the hydrogel force and displacement on the actuating magnet was dictated by the initial hydrogel size and the wall constraint, ii) the critical hydrogel height was dictated by the initial spring magnet position relative to the latch magnet in the hybrid actuator, and iii) the output force of the actuator was dictated by the net force on the spring magnet. By manipulating these parameters, the hydrogel actuators can be tailored to automatically trigger multiple magnetic mechanisms simultaneously or in series to generate complex multi-step motions depending on pH. In doing so, the exploration of an extensive array of kinematics when designing millimeter-scale robotic devices is possible.

5. Experimental Section/Methods

Synthesis of the agar-poly(acrylic acid) hydrogels: Agar-poly(acrylic acid) hydrogel was prepared by heating 0.205 g agar in 4 mL deionized water (DI water) to 85 – 90 °C. When the agar was cooled down to 50 – 60 °C, acrylic acid (2.8 mL, Sigma-Aldrich Canada Co., Canada), diphenyl(2,4,6- trimethylbenzoyl)phosphine oxide 97% (0.015 g, Sigma-Aldrich Canada Co., Canada), and polyethylene glycol diacrylate 700 (29 μL, Sigma-Aldrich Canada Co., Canada) were quickly added and mixed by a stirring rod. Then the mixture was poured on a glass slide with rubber mold and cooled for ~10 min prior to the sample curing. The glass slide was then transferred to an ultraviolet (UV) curing system described in Xu *et al*. [25] The material was cured into cylinders with 3-4 mm in diameter or cubes with 1.42 mm in side length under a 405 nm light source. Each geometry was cured for 6 cycles with every cycle of 10 seconds. The cured samples were subsequently rinsed with DI water thrice and soaked in DI water for 3 days, and then transferred into isopropyl alcohol (IPA) for 1 day to remove impurities. Finally, the samples were dried in the air under room temperature and placed in a vacuum chamber for 4 days before swelling tests.

Making 0.01 M phosphate buffer solution at varying pH: Phosphate buffer solutions were made by adding monobasic potassium phosphate (Sigma-Aldrich Canada Co., Canada) in DI water to make 0.01 M solutions. The pH was then adjusted by either 1 M of NaOH or HCl to achieve solutions with pH of 2.2, 3, 4, 4.8. 6, 6.8, 7.4, and 9.

Hydrogel swelling tests: The free swelling ratio of the hydrogel at equilibrium was characterized by immersing samples in 0.01 M phosphate solution with varying pH, simulated gastric fluid (SGF, pH 1.2 and 0.05 M salt solution), and simulated intestinal fluid (SIF, pH 6.8 and 0.10 M salt solution). SGF and SIF were made based on the Test Solutions (TS) in the U.S. Pharmacopeia. [26] The initial masses of dry hydrogels were first measured. Then the samples were immersed in the solutions for ~4 days to ensure equilibrium swelling. The

residual fluids on the surface were removed by lightly patting the hydrogel with Kimwipes (Kimberly-Clark Professional, USA) prior to the final mass measurement. The volumetric free swelling ratio was then calculated by Equation 1.

Compression and dynamic mechanical tests: The uniaxial compression tests were implemented using 500 N and 2000 N load cells with a crosshead speed of 1 mm·min^{-1} on an Instron 5800 under room temperature. The hydrogels used for the tests were free swelled cylinder-shaped hydrogels in pH 2.2, 6, and 7.4 phosphate buffer solution (0.01 M) after at least 3 days. The stress-strain data from the compression tests were used to determine the elastic stress contributions of polymer network in the analytical hydrogel model as seen in the Supplementary Information Figure S1.

Rheology tests were conducted for the hydrogel by implementing an amplitude sweep using a rheometer (DH3 interfacial rheometer, TA Instruments) to determine the linear viscoelastic region at low frequency and show the viscoelastic behavior of the hydrogel at varying pH values. To match the shape of the rheometer top plate, the pre-gel solutions were poured into a circular silicone rubber mold and polymerized using a UV flashlight for 6 cycles at 10 second intervals. The hydrogels were soaked in DI water for 3 days with water being changed every day. It was then soaked in IPA to remove remaining impurities, dried at room temperature, and then placed into vacuum for 3 days. The hydrogels were then either immersed in pH 2.2, 6, or 7.4 phosphate buffer solutions (0.01 M) for 3 days resulting in an approximate swelled diameter of 40 mm. A flat top plate with diameter of 40 mm was used on the hydrogel, and the axial force was kept constant at 4.8-5 N. The frequency was set to 1 Hz and the temperature was set to 20 °C. All the results were shown in Supplementary Information Figure S3.

Hydrogel blocking force tests: The blocking force of the hydrogel was measured using 0.5-5 kg load cells. A 35 mm diameter petri dish was placed on top of the load cell to hold a cylinder-shaped hydrogel in the center. A cylinder probe was attached to a metal L-bracket which was screwed onto a vertically placed positioning slide to adjust the height of the probe relative to the top of the hydrogel. The probe was positioned so that it touched the top surface of the dried hydrogel with no force. The pH solution was then poured into the petri dish to measure the force of the hydrogel as it swelled. A layer of silicone oil (20 cSt, Sigma-Aldrich Canada Co., Canada) was added on top of the pH solution to prevent evaporation. The blocking force at varying pH was measured for ~72 hours when the hydrogel was fully swelled and equilibrium was reached.

Actuator Tests: The body of the hybrid hydrogel-magnet actuator was a 3D-printed square tube with dimensions equal to the specified wall constraints to house the cube hydrogel and the actuating magnet (Clear V4, FormLabs Inc., MA, USA). The latch magnet was glued to the bottom of the tube. The average side length of the cube hydrogels was 1.42 ± 0.03 mm (mean ± standard deviation, n = 4). The actuator with and without the actuating magnet and the actuator with the spring magnet mechanisms were immersed in SGF or SIF for at least 48 hours to ensure equilibrium swelling. All magnets were N52 grade (SuperMagnetMan, AL, USA). A long equilibration time was used since the hydrogel model is only valid for hydrogels at equilibrium. The SGF has a pH of 1.2 and an approximate salt concentration of 0.05 M, and the SIF has a pH of 6.8 and an approximate salt concentration of 0.10 M. Table 1 lists all the actuator tests with varying hydrogel geometries, wall constraints, loading conditions and pH solutions. Each actuator test was conducted once due to the long duration of the experiment.

For each experiment, the hydrogel heights at the initial state and at equilibrium were measured four times (n = 4) from captured images using ImageJ software and labelled in pixels as p_0 and p, respectively. The heights were then converted to millimeters using the millimeter-to-pixel conversion ratio. (Note: the cube magnet side length was used as the reference length for the conversion ratio computation.) The millimeter-to-pixel conversion ratios were computed as the average of four measurements (n = 4, unit of $mm \cdot px^{-1}$) and were labelled as a_0 and a for the images at the initial state and at equilibrium, respectively. The normalized hydrogel height along axis 3 (λ_3) was calculated using Equation 10. An error propagation was then performed on the calculated λ_3 to approximate the standard deviation of λ_3 (Equation 11).

$$\lambda_3 = \frac{h_3}{h_0} = \frac{pa}{p_0 a_0} \qquad (10)$$

$$\text{Standard deviation of } \lambda_3 = \sqrt{\left(\frac{\delta\lambda_3}{\delta p}\delta p\right)^2 + \left(\frac{\delta\lambda_3}{\delta a}\delta a\right)^2 + \left(\frac{\delta\lambda_3}{\delta p_0}\delta p_0\right)^2 + \left(\frac{\delta\lambda_3}{\delta a_0}\delta a_0\right)^2} \qquad (11)$$

where δp, δp_0, δa, δa_0 are the standard deviations of the measurements and $\frac{\delta\lambda_3}{\delta p}, \frac{\delta\lambda_3}{\delta a}, \frac{\delta\lambda_3}{\delta p_0}, \frac{\delta\lambda_3}{\delta a_0}$ are the partial derivatives of Equation 10.

Table 1: Summary of experiments with varying hydrogel geometries, wall constraints, magnetic loads, and pH solutions

Experiment	Wall Constraints	With Magnetic Load?	Solution
Actuator with cube hydrogel	$w_1 = w_2 = 2.79$	No	SGF & SIF
Actuator with cube hydrogel	$w_1 = w_2 = 2.79$	Yes (3 mm cube magnet load)	SGF & SIF
Rotating mechanism with cube hydrogel	$w_1 = 1$, unconstrained w_2 in SGF, $w_1 = w_2 = 2.79$ in SIF	Yes (2 mm cube magnet load + one 2 mm spring magnet load)	SGF & SIF
Translational mechanism with cube hydrogel	$w_1 = 1$, unconstrained w_2 in SGF, $w_1 = w_2 = 2.79$ in SIF	Yes (2 mm cube magnet load + two 2 mm spring magnet load)	SGF & SIF

An additional note regarding the actuator experiments is that the simulated gastric fluid can corrode the magnet if there are any scratches or fractures on the nickel coating. The occurrence of corrosion was demonstrated by the rust on the scratched magnet and the appearance of bubbles in SGF as time passed. To prevent corrosion, the magnet should be fully encapsulated by acid-resistant material in the future.

Friction of magnet against actuator wall: The static coefficient of friction (c_f) of the magnet against the wall of 3D printed square tube made of UV resin (Clear V4, FormLabs Inc., MA, USA) was determined by placing the magnet on an incline at varying angles. The incline was printed with the same UV resin, layer resolution and stacking direction as the square tube to ensure the same surface roughness. The angle at which the force of gravity of the magnet overcame the static friction to start sliding was recorded as α. The static coefficient was then computed as Equation 9.

The coefficient can be used to approximate the critical static friction force ($F_{f,cr}$) that impedes the spring magnet triggering.

$$F_{f,cr} = c_f F_N \qquad (12)$$

where F_N is the normal force to the surface.

Magnetic force modeling and validation: The magnetic force between two permanent magnets was modeled using the dipole model in tensor notation. Given all magnets would be

the same size in the actuator system, $|m_a| = |m_b| = |m|$. Each magnet can be divided into evenly distributed small components. Each component can be approximated as a magnetic dipole and the overall magnetic force between two magnets is the sum of the interaction force between each pair of the dipoles as,

$$F_{ab_i} = \frac{3\mu_0|m|^2}{4\pi|r|^4}\left[\hat{r}_i\left(\hat{m}_{a_i}\hat{m}_{b_i}\right) + \hat{m}_{a_i}\left(\hat{r}_i\hat{m}_{b_i}\right) + \hat{m}_{b_i}\left(\hat{r}_i\hat{m}_{a_i}\right) - 5\hat{r}_i(\hat{r}_i\hat{m}_{a_i})(\hat{r}_i\hat{m}_{b_i})\right] \quad (13)$$

where F_{ab_i} is the force of *b* on *a* in the principal direction *I* of the Cartesian coordinates, m_{a_i} and m_{b_i} are the magnetic moment of two dipoles in the principal direction *I*, r_i is the position in the principal direction *I*, μ_0 is the vacuum permeability.[20] The annotation of $|\cdot|$ is the Euclidean norm, and $\hat{\cdot}$ is the unit vector.

In our magnetic dipole model, each permanent magnet was divided into at least 150 individual dipoles evenly spaced throughout the width and the height of the magnet. The magnetic interaction force between two magnets was calculated by summing all interacting forces between the dipoles in magnet *a* and all the dipoles in magnet *b*. For the experimental measurements of the magnetic force between two 3 mm cube magnets, one cube magnet was fixed to a positioning stage, and the other was fixed on a load cell. The smallest separation distance between the closest faces of two magnets was 0.4 mm and the largest was 9.0 mm. Meanwhile, a finite element model was developed in COMSOL for the simulated computation of the magnetic forces between two cube magnets. It can be observed from Figure 1(f) that the curves of the magnetic dipole model, the simulation and the experimental result fit well with each other.

Supporting Information

Supporting Information is available from the Wiley Online Library or from the author.

Acknowledgements

The authors gratefully acknowledge the financial support provided by the Natural Sciences and Engineering Research Council of Canada (NSERC). The authors also thank Victor Sit for the assistance on the hydrogel rheology tests, Anastasia Aubeeluck for the assistance on the compression tests and Jia Xi Chen for advising on the finite element analysis.

Received: ((will be filled in by the editorial staff))

Revised: ((will be filled in by the editorial staff))

Published online: ((will be filled in by the editorial staff))

References

[1] A. Doroudchi, R. Khodambashi, M. Sharifzadeh, D. Li, S. Berman, D. M. Aukes, *IEEE Robot. Autom. Lett*. **2021**, *6*, 4774.

[2] Y. Sun, L. Chen, Y. Jiang, X. Zhang, X. Yao, S. Soh, *Mater. Horiz.* **2019**, *6*, 160.

[3] A. K. Mishra, T. J. Wallin, W. Pan, P. Xu, K. Wang, E. P. Giannelis, B. Mazzolai, R. F. Shepherd, *Sci. Robot*. **2020**, *5*, eaaz3918.

[4] Y. Dong, J. Wang, X. Guo, S. Yang, M. O. Ozen, P. Chen, X. Liu, W. Du, F. Xiao, U. Demirci, B.F. Liu, *Nat. Commun*. **2019**, *10*, 4087.

[5] S. Xiao, M. Zhang, X. He, L. Huang, Y. Zhang, B. Ren, M. Zhong, Y. Chang, J. Yang, J. Zheng, *ACS Appl. Mater. Interfaces*. **2018**, *10*, 21642.

[6] X. Liu, C. Steiger, S. Lin, G. A. Parada, J. Liu, H. F. Chan, H. Yuk, N. V. Phan, J. Collins, S. Tamang, G. Traverso, X. Zhao, *Nat. Commun*. **2019**, *10*, 493.

[7] A. Nojoomi, H. Arslan, K. Lee, K. Yum, *Nat. Commun*. **2018**, *9*, 3705.

[8] M. Li, X. Wang, B. Dong, M. Sitti, *Nat. Commun*. **2020**, *11*, 3988.

[9] Q. L. Zhu, C. Du, Y. Dai, M. Daab, M. Matejdes, J. Breu, W. Hong, Q. Zheng, Z. L. Wu, *Nat. Commun*. **2020**, *11*, 5166.

[10] X.C. Sun, H. Xia, X.L. Xu, C. Lv, Y. Zhao, *Sens. Actuators B Chem*. **2020**, *322*, 128620.

[11] Z. Shao, S. Wu, Q. Zhang, H. Xie, T. Xiang, S. Zhou, *Polym. Chem.* **2021**, *12*, 670.

[12] C. Yang, F. Su, Y. Xu, Y. Ma, L. Tang, N. Zhou, E. Liang, G. Wang, J. Tang, *ACS Macro Letters*. **2022**, *11*, 347.

[13] T. Nonoyama, J. P. Gong, *Annu. Rev. Chem. Biomol. Eng*. **2021**, *12*, 393.

[14] A. K. Means, M. A. Grunlan, *ACS Macro Letters* **2019**, *8*, 705.

[15] L. Hines, K. Petersen, G. Z. Lum, M. Sitti, *Adv. Mater*. **2017**, *29*, 1603483.

[16] M. A. Woodward, M. Sitti, *IEEE Trans. Robot*. **2019**, *35*, 589.

[17] M. A. Woodward, M. Sitti, *IEEE Trans. Magnet*. **2018**, *54*, 1.

[18] T. Tanaka, D. J. Fillmore, *J. Chem. Phys.* **1979**, *70*, 1214.

[19] H. Yuk, S. Lin, C. Ma, M. Takaffoli, N.X. Fang, X. Zhao, *Nat. Commun.* **2017**, *8*, 14230.

[20] K.W. Yung, P.B. Landecker, D.D. Villani, *Magn. Electr. Sep.* **1998**, *9*, 39.

[21] W. R. K. Illeperuma, J.Y. Sun, Z. Suo, J. J. Vlassak, *Soft Matter* **2013**, *9*, 8504.

[22] H. Na, Y.W. Kang, C. S. Park, S. Jung, H.Y. Kim, J.Y. Sun, *Science* **2022**, *376*, 301.

[23] R. Marcombe, S. Cai, W. Hong, X. Zhao, Y. Lapusta, Z. Suo, *Soft Matter* **2010**, *6*, 784.

[24] W. Hong, Z. Liu, Z. Suo, *Int. J. Solids Struct*. **2009**, *46*, 3282.

[25] T. Xu, J. Zhang, M. Salehizadeh, O. Onaizah, E. Diller, *Sci. Robot*. **2019**, *4*, eaav4494.

[26] United States Pharmacopeia and National Formulary (USP 42-NF 37), United States Pharmacopeial Convention, Rockville, MD, **2019**.

Table of contents entry:

The pH-responsive hydrogel blocking force and constrained swelling can be predicted to design actuators that automatically trigger fast magnetic mechanisms in small-scale devices without onboard power. The hybrid hydrogel-magnet actuator is shown to drive rotational and translational magnetic mechanism by the addition of spring magnets.

TOC figure:

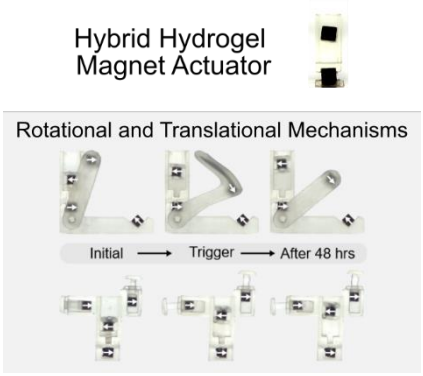

Y.P. Lai, Z. Li, H. Naguib, E. Diller*

Hybrid Hydrogel-Magnet Actuators with pH-responsive Hydrogels for Gastrointestinal Microrobots